Magnetic Resonance in Medicine 42:526–540 (1999)

Color Schemes to Represent the Orientation of Anisotropic Tissues From Diffusion Tensor Data: Application to White Matter Fiber Tract Mapping in the Human Brain

Sinisa Pajevic[1] and Carlo Pierpaoli[2]*

This paper investigates the use of color to represent the directional information contained in the diffusion tensor. Ideally, one wants to take into account both the properties of human color vision and of the given display hardware to produce a representation in which differences in the orientation of anisotropic structures are proportional to the perceived differences in color. It is argued here that such a goal cannot be achieved in general and therefore, empirical or *heuristic* schemes, which avoid some of the common artifacts of previously proposed approaches, are implemented. Directionally encoded color (DEC) maps of the human brain obtained using these schemes clearly show the main association, projection, and commissural white matter pathways. In the brainstem, motor and sensory pathways are easily identified and can be differentiated from the transverse pontine fibers and the cerebellar peduncles. DEC maps obtained from diffusion tensor imaging data provide a simple and effective way to visualize fiber direction, useful for investigating the structural anatomy of different organs. Magn Reson Med 42:526–540, 1999. © **1999 Wiley-Liss, Inc.**

Key words: diffusion; tensor; color; white matter; MRI; anisotropy; brain; human

In recent years, MRI has increasingly been used to study tissue water diffusion in vivo. By acquiring diffusion-weighted images with diffusion gradients oriented in at least six noncollinear directions, it is possible to measure the diffusion tensor (**D**) in each voxel (1,2). Diffusion tensor data can, in turn, be used to compute quantities that characterize specific features of the diffusion process, such as the trace of the tensor [Trace(**D**)], indices of diffusion anisotropy, and the principal directions of diffusion (eigen vectors of **D**) (See Ref. 3 for a review). Trace(**D**), which is proportional to the orientationally averaged water diffusion coefficient, can better delineate ischemic and infarcted brain regions than single-direction apparent diffusion coefficients (4,5). Anisotropy measures yield information about the structure of normal and pathological white matter that cannot be obtained from conventional, relaxometry-based MRI (6,7). The principal directions of diffusion provide information on the spatial orientation of anisotropic structures that may be useful to further characterize tissue structural anatomy. For example, in studying cardiac and skeletal muscle fibers, direction mapping might provide insight about the relationship between the structure of the muscle tissue and its function during different physiological and pathological conditions (8–11). Most of what we know in this regard has been derived from invasive procedures on isolated organs. In the brain, fiber direction mapping is useful to identify and differentiate anatomical white matter pathways that have similar structure and composition but different spatial orientation (12,13). Historically, such studies of the brain's structural anatomy have been performed only with histological methods.

While Trace(**D**) and anisotropy measures are scalar quantities, easily displayed using gray scale maps, representing the directional information contained in the diffusion tensor is more problematic. Previously proposed approaches include: gray scale maps of the polar and azimuthal angles of the eigenvector associated with the largest eigenvalue of the diffusion tensor ($\mathbf{V}_{max}$) (14,15); two-dimensional (2D) line fields of the in-plane projection of $\mathbf{V}_{max}$ (16); display of diffusion ellipses (17) and octahedra (8,9); and three-dimensional (3D) rendering of diffusion ellipsoids (6,18–20) in each voxel. Theoretically, these are rigorous approaches but they face the problem of visualizing 3D objects in two dimensions. For example, cigar-shaped diffusion ellipsoids would be indistinguishable from spheres if the anisotropic structure is pointing at the viewer (i.e., the largest diffusivity is parallel to the viewing axis). Displaying fiber direction using 3D rendering of diffusion ellipsoids or other solids could be substantially improved by viewing the structure from many different angles using computerized animation. Still, 3D rendering is suitable to display only small portions of an image and is cumbersome for global viewing of an entire image or a series of images.

Other methods to visualize fiber direction have used colors (21–26). Some of these methods assign different color components to diffusion-weighted images (DWI) or apparent diffusion coefficient (ADC) maps acquired with gradients applied in perpendicular directions (21,23). As acknowledged by the authors who proposed these schemes, these nontensor-based approaches fail to correctly describe fiber direction when **D** has nonzero off-diagonal elements, a condition often encountered in biological tissues (15,20). It has been suggested that a color RGB representation of the components of $\mathbf{V}_{max}$, weighted, or filtered, by some measure of diffusion anisotropy, may provide a concise and effective way to display the directions of anisotropic structures in a single image (25,26). Using directionally

[1]Mathematical and Statistical Computing Laboratory, Center for Information Technology, National Institutes of Health, Bethesda, Maryland.

[2]Neuroimaging Branch, National Institute of Neurological Disorders and Stroke, National Institutes of Health, Bethesda, Maryland.

*Correspondence to: Carlo Pierpaoli, Section of Tissue Biophysics and Biomimetics, NIH/NICHD/LIMB, Building 13, Room 3N17, 13 Center Drive, Bethesda, MD 20892-5766. E-mail: carlo@helix.nih.gov

Received 27 October 1998; revised 21 May 1999; accepted 24 May 1999.

encoded color (DEC) maps is appealing because it facilitates displaying the orientation of fibers that run at an angle to the image plane. Previously proposed tensor-based DEC schemes (25,26) overcome the problems inherent in DWI- or ADC-based schemes, but still have limitations that preclude them from reliably and quantitatively representing fiber direction (see Background section below). Here we propose improved tensor-based DEC mapping schemes that produce a simple, intuitive, and faithful representation of fiber direction. Finally, we use these schemes to identify and display white matter fiber tracts in the normal human brain.

BACKGROUND

We present some objectives that we think should be considered in designing a tensor-based quantitative color representation of fiber direction: (a) Perceived color differences should be proportional to actual differences in direction, characterized either by the Euclidian distance between vectors or by the angle between them. (b) Fiber orientation should be specified in an anatomically based coordinate system, independent from the laboratory reference frame in which the tensor dataset is acquired. (c) Only the directional information contained in the $\underline{\mathbf{D}}$ should be displayed, and the representation should not be affected by parameters related to the magnitude of diffusivity, such as Trace($\underline{\mathbf{D}}$) or diffusion coefficients. Some measure of anisotropy, however, could be used as a mask or filter to avoid representing directions in isotropic structures in which defining a fiber tract direction would be meaningless (25,26). (d) Commonly identifiable color groups (e.g., red, green, blue, yellow, cyan, magenta, etc.) should be approximately associated with a characteristic direction (e.g., direction along x, y, z, directions bisecting the xy, yz, xz planes, etc.).

Previously proposed DEC schemes (25,26) satisfy only a few of these requirements and, in particular, do not address the issues of points (a) and (b) above. To design improved DEC schemes, we investigated three sources of misrepresentation: (i) nonlinear effects of the display device, (ii) properties of human color vision, and (iii) antipodal symmetry of the eigenvectors of $\underline{\mathbf{D}}$.

Nonlinear Effects of the Display Device (Gamma Correction)

For a particular color to have the same appearance on different devices, one has to use a device-independent color specification [e.g., CIE XYZ[1] system (27)]. This is attained through linear transformations of the primary colors for different devices (28). The next step is to account for the nonlinear relationship existing between the true luminosity produced by the device, L, and the digital values stored in the frame buffer, f (29). For each color channel of a cathode ray tube (CRT), this relationship can be written in the simplest form as $L \sim f^{\gamma}$, where γ is the characteristic exponent for a given channel. Once the relationship is determined, one can apply a correction known as the *gamma correction*. When applying this correction, one has to ensure that the display software or the hardware look-up tables are not already performing it. Typical values for γ are $\gamma \in [2.0, 2.4]$ for almost all CRT-based computer displays except for Macintosh ($\gamma \cong 1.5$) and SGI ($\gamma \cong 1.3$) computer displays. The formula is primarily derived for the CRT device, but is frequently applied to other devices, using different parameter values. With the advent of new display hardware, the nature of the nonlinear relationship can become quite different.

Properties of Human Color Vision

In order to construct a color representation scheme in which perceived color differences are proportional to actual differences in direction, we must consider not only the properties of the display device, but also the properties of our color vision. Throughout the history of color research, attempts have been made to define color ordering schemes based on the perceived difference between colors. Although color spaces have metric properties, the goal to find a uniform color space in which the perceived color difference is proportional to the Euclidean distance in such a space has remained elusive. Moreover, in complex scenes, such as color medical images, color perception involves the perception of contrast, i.e., the perceived color in a given region is influenced by the color of all the surrounding regions. Using the retinex model (30), one can predict the perceived color qualities for any region of a given image. However, constructing color mapping schemes based on the retinex theory having general validity for different images is impossible. If we ignore the effects of contrast, a perceptually uniform color representation can be constructed using approximately uniform color spaces, such as the CIEL*u*v* color space (27). Even a less elaborate approach should not ignore some fundamental relationships in color perception, such as the simple nonlinear relationship between the true luminosity of monochromatic light and its perceived brightness (Steven's law).

Antipodal Symmetry of the Eigenvectors of $\underline{\mathbf{D}}$ (Discontinuity Artifacts)

The sign of the eigenvectors of $\underline{\mathbf{D}}$ is arbitrary since the parallel and anti-parallel vectors convey the same information ($\mathbf{V_{max}} \equiv -\mathbf{V_{max}}$). In statistics, directional data with such antipodal symmetry are referred to as *axial data*. To have a unique vector representation of axial data, the vectors have to be mapped to only one hemisphere in a spherical coordinate system. The plane that divides the spherical coordinate system into two hemispheres can be positioned in an arbitrary direction; however, within this plane, fiber orientation will still be represented by two antipodally symmetric vectors $\mathbf{V_{max}}$ and $-\mathbf{V_{max}}$. We call this *the plane of discontinuity* because a color representation mapped on the surface of a sphere will be discontinuous at the intersection of the sphere with this plane (see Fig. 1). For any structure oriented nearly parallel to the plane of discontinuity a small change in orientation can cause the $\mathbf{V_{max}}$ to cross the plane of discontinuity and be represented with a very different color. This small change in orientation of the structure in the neighboring voxels can result from the natural curvature of the structure or can be due to noise in measuring $\mathbf{V_{max}}$. In general, a continuous

[1]CIE stands for Commission Internationale de L'Eclairage (International Color Commission). The three letters following CIE indicate the type of color coordinates used in a given color system.

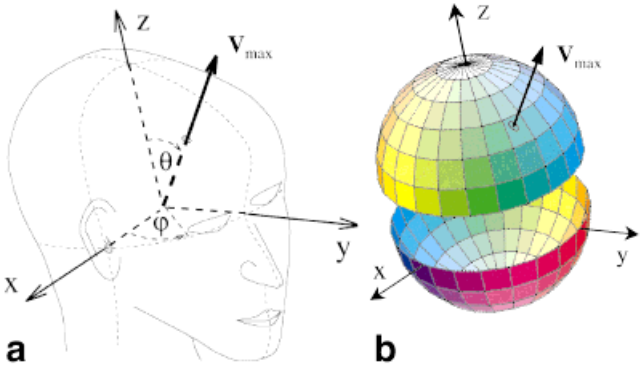

FIG. 1. **a:** Definition of the anatomical reference frame for brain images. The yz plane corresponds to the sagittal plane aligned with the interhemispheric fissure; the y axis corresponds to the anterior-posterior intercommissural line. The x, y, and z axes orientation is as shown in the figure. **b:** Color representation sphere for the no symmetry scheme described in Materials and Methods. The sphere is anchored to the anatomic reference frame; thus, for a given scheme, an anisotropic structure will have the same color independent of the view (axial, coronal, or sagittal). The figure also shows how $\mathbf{V}_{max}$ for a generic direction is mapped on the color sphere.

metric space for directional data with antipodal symmetry cannot be constructed; hence, the metric properties of the color spaces cannot be used for representation. However, a metric can be constructed if we assign zero distance, and therefore the same color, to all vector pairs that satisfy a 2-fold rotational symmetry around the z axis (i.e., all vector pairs that are images of each other under 180° rotations). In such case, the antipodally symmetric vector pairs lying within the plane of discontinuity will correctly have the same representation.

MATERIALS AND METHODS

Color Representation of Fiber Orientation

We assumed that the orientation of fibers is described by the eigenvector associated with the largest eigenvalue, $\mathbf{V}_{max}$. We established a coordinate system fixed to defined anatomical landmarks (Fig. 1a) satisfying the condition (b) described in the Background section. Proper rotations were used to convert from the laboratory reference frame to the specified anatomical reference frame. The eigenvector $\mathbf{V}_{max}$ is a unit vector completely determined by its polar (θ) and azimuthal (φ) angles that are defined within the anatomical coordinate system as shown in Fig. 1a. When no anisotropy filter is used, a particular color representation can be shown on a unit sphere, which we call the *color representation sphere*. Figure 1b shows the color representation sphere for the *no symmetry* scheme described later in this section. As mentioned before, fiber orientation is described by two vectors $\mathbf{V_{max}}$ and $-\mathbf{V_{max}}$, or two pairs of angles (θ,φ) and $(\pi-\theta,\varphi+\pi)$, and only the vectors in one of the two hemispheres are used for unique representation. Unless stated otherwise, vectors are expressed in the upper hemisphere ($z>0$ or $0\leq\theta\leq\pi/2$) and the xy plane is the plane of discontinuity. The lower hemisphere is just an antipodally symmetric copy of the upper hemisphere, as shown in Fig. 1b in which the color representation sphere is split along the plane of discontinuity.

As in previously proposed schemes (25), the brightness of our DEC maps is weighted by a measure of diffusion anisotropy to avoid representing isotropic or slightly anisotropic structures in which $\mathbf{V}_{max}$ will have virtually random orientation. The anisotropy measure we used is the *lattice* index, Λ (20), which is a linear combination of its basic elements Λ_N, defined as:

$$\Lambda_N = \frac{\sqrt{3}}{\sqrt{8}}\frac{\sqrt{D_{ref}:D_N}}{\sqrt{D_{ref}:D_N}} + \frac{3}{4}\frac{D_{ref}:D_N}{\sqrt{D_{ref}:D_{ref}}\sqrt{D_N:D_N}} \qquad [1]$$

where $D_{ref} : D_N$ denotes the tensor dot product between the diffusion tensor of the given voxel D_{ref}, and that of the neighboring voxel D_N. *D* (italic) indicates the anisotropic part the diffusion tensor or *deviatoric* tensor. The formula of the basic elements of the lattice index is reported here because it contained typographical errors in the original publication (20). A more detailed description of the quantities appearing in the formula and the properties of the lattice anisotropy index are reported in reference (20). We implemented two types of anisotropy filters in our color representations. In the first one, each of the color components contains a weighting factor Λ_w, which linearly increases from 0 to 1 within a specified range of lattice index values $\Lambda\in[\Lambda_{min},\Lambda_{max}]$. In the second, only structures where the lattice index is larger than Λ_{min} are represented; the others are truncated and set to black (see Appendix A for details).

Color Maps and Symmetry Considerations

To reduce the discontinuity artifacts mentioned in (iii) of the Background section, we allowed different directions to be represented with the same color if some form of symmetry exists between these directions. In this case, we have an orientational ambiguity because the color representation of orientation is not unique. In some situations, however, using such symmetries is justified by existing symmetries in the imaged anatomy. With regard to which type of symmetry is used, we distinguished the following cases:

No Symmetry. This representation is implemented by relating the azimuthal angle of the vector (φ) to color hue and the polar angle ($\theta \leq \pi/2$) to color saturation. For example, a simple implementation in HSV (Hue, Saturation, Value) color space is $H = \varphi$, $S = 2\theta/\pi$, $V = \Lambda_w$. This representation is unique because a particular color describes a single direction but suffers from discontinuity artifacts.

Rotational Symmetry (2-Fold). In this color representation any vector and its pair rotated by 180° around the z axis will have the same color representation [$\mathbf{V_{max}}(\theta,\varphi) \equiv \mathbf{V_{max}}(\theta,\varphi+\pi)$, or $\mathbf{V_{max}}(v_x,v_y,v_z) \equiv \mathbf{V_{max}}(-v_x,-v_y,v_z)$]. This representation is implemented in a fashion similar to the *no symmetry* approach but with the constraint $H(\varphi) = H(\varphi+\pi)$. This scheme removes the discontinuity artifacts but does not provide a unique representation of directions and is, also, perceptually highly nonuniform (see Table 1 for a summary of the properties of different color schemes).

Mirror Symmetry. The mirror symmetric representation implies that any two vectors that are mirror images of each other relative to the yz plane of the anatomical coordinate

Table 1
Properties of Color Maps*

	Absolute value	Rotational symmetry	Mirror symmetry	No symmetry	Preferred direction
Discontinuity artifacts	None	None	Moderate	Severe	Severe but avoidable
Perceptual uniformity	Good	Very poor	Poor	Good	Good
Orientational ambiguity	Severe (4)	Moderate (2)	Moderate (2)	None	None for $\theta < \theta_C$

*Summary of the properties of different color mapping schemes. We consider a) the presence and degree of discontinuity artifacts; b) whether a good perceptual uniformity can be achieved using the heuristic or unifor color space approach; and c) the presence and degree of orientational ambiguity or nonuniqueness of the color representation (i.e., whether or not different orientations are represented by the same color). The maximal number of orientations that are represented by the same color is reported in the parentheses. Note that in schemes suffering from orientational ambiguity there are still specific colors that provide a unique representation, such as red, green, and blue in the *absolute value* scheme, or white and all the fully saturated hues in the *rotational symmetry* scheme.

system will have the same color representation [$\mathbf{V_{max}}(-v_x,v_y,v_z) \equiv \mathbf{V_{max}}(v_x,v_y,v_z)$]. Mirror symmetry exists between many structures in the left and the right brain hemispheres.

Absolute Value. Simultaneously assuming the existence of mirror and rotational symmetries together with the inherent antipodal symmetry ($\mathbf{V_{max}} \equiv -\mathbf{V_{max}}$), implies that the sign of any vector component is unimportant; only the absolute value is. This yields a simple representation in RGB color space in which RGB components are associated with the absolute value of the components of the vector, as originally proposed in (25), i.e.:

$$R = \Lambda_w|v_x|,\ G = \Lambda_w|v_y|,\ B = \Lambda_w|v_z|$$

Preferred Direction. When no symmetry is assumed and the structure of interest lies close to the plane of discontinuity, it is desirable to rotate the coordinates of the color space so that undesirable artifacts are shifted to a different plane. For a given region of interest (ROI), we determine the dominant fiber direction, or we specify a particular direction that we want to explore. This is called the *preferred direction* and is described by the vector $\mathbf{v}_p$. Once a preferred direction is selected, the *no symmetry* representation is implemented in the new coordinate system in which the new z axis coincides with $\mathbf{v}_p$ (see Appendix A for details) and the discontinuity artifacts are now shifted to a plane perpendicular to $\mathbf{v}_p$. Very often one is only interested in the structures along the chosen preferred direction and not in those close to the plane of discontinuity. Hence, we chose a single cutoff polar angle θ_C (usually between 70° and 80°) to define the structures to be color coded ($\theta \leq \theta_C$). Structures having $\theta > \theta_C$, i.e., lying close to the plane where discontinuity artifacts occur, are displayed in black. Alternatively, one can use a cone defined by the preferred direction and a smaller angle ($\theta_C < 70°$) to increase the resolving power of the color representation around the direction of $\mathbf{v}_p$. Only with the preferred direction approach is it appropriate to use the cutoff angle θ_C since in the other schemes previously described, the plane of discontinuity is fixed and the same structures would always be eliminated.

Color Perception Considerations

We used two different approaches to address the properties of color perception. The first was based on the uniform color spaces CIEL*u*v* and CIEL*a*b* (27), and the second was an heuristic approach in which desirable properties were obtained empirically.

Uniform Color Space Approach. By using uniform color spaces, we hoped to improve the color representation despite the fundamental limitations described in (ii) of the Background section. Only the *no symmetry* and *absolute value* cases can be implemented within uniform color space in a relatively simple way and their implementation is briefly described in Appendix C.

Heuristic Approach. In order to alleviate some of the most pronounced artifacts associated with color display and perception [(i) and (ii) of the Background section], we propose schemes in which a perceptually satisfying representation is obtained interactively by adjusting a small number of parameters. These are called heuristic parameters to emphasize the empirical nature of this approach. These heuristic parameters are listed in Table 2 and a detailed explanation of their implementation is found in Appendix A. We used heuristic parameters p_B, p_E, and L_E to achieve approximately uniform brightness for different colors; p_β to modify the nonlinear relationship between the perceived brightness and the anisotropy measure; and p_S to modify the dependence between the saturation and the angle θ. Parameter p_C is used so that $p_C = 0$ yields the maximal range of colors without regard to uniform brightness (p_B, p_E, and L_E are ineffective); $p_C = 1$ reduces the range of colors but allows a more faithful representation of anisotropy and a more uniform color representation. We also treated as heuristic parameters both the gamma correction exponent γ and the Steven's law exponent β, which describes the nonlinear relationship between the luminosity and perceived brightness.

Color Circles

Color circles were constructed by projecting the color representation sphere onto the viewing plane using the equal area Lambert projection (Fig. 2b). These color circles are useful to relate a particular color in the DEC map with its corresponding fiber orientation. For axial images the representation sphere is viewed from below (negative z axis of our anatomical coordinate system pointing at the viewer, see Fig. 2b) and for coronal images from the front (positive y axis pointing at the viewer, see Fig. 2b), according to the standard convention for viewing MR images. A grid of parallels and meridians is added to the circle at 15° intervals to indicate the angles θ_v (angle at which the structure is positioned relative to the viewing

Table 2
List of Heuristic Parameters*

Parameter symbol	Short description of the parameter	Range of suggested (upper field) and allowed (lower field) values
p_B	Decreases the saturation of blue hues to achieve better uniformity of perceived brightness for different hues, and more faithful representation of diffusion anisotropy.	[0, 0.3/p_E] [0, 0.5/p_E]
p_E	Used for equalization of the perceived brightness. For $p_E = 0$ RGB components are treated as equivalent; for $p_E = 1$ the components are weighted differently to achieve uniform brightness for different hues, similar to CIEL*u*v*.	[0, 1]
L_E	Reference brightness to which colors are scaled. For higher values of L_E the larger values of p_B should be used and vice versa. For large L_E the equivalent of p_B for red should be used.	[0.6, 0.7] [0, 1]
p_C	Control parameter. For $p_C = 0$ the maximal range of colors is used and uniformity is ignored (p_B, p_E, and L_E are disabled); for $p_C = 1$, p_B, p_E, and L_E are fully enabled and a smaller color range is used.	[0, 1]
p_S	Modifies the relation between the hue and angle θ in HSV-based schemes; $p_S > 0$. For $p_S \cong 0$ relationship is linear. We use $p_S \cong 0.5$.	(0, 1]
p_β	Modifies the exponent of the anisotropy index-based weighting factor (Λ_w). When $p_\beta < 1$, structures with low anisotropy are emphasized.	[0.5, 1] (0, ∞)
β	Parameter based on Steven's law exponent relating true luminosity and perceived brightness.	[0.3, 0.5] (0, ∞)
γ	Parameter based on gamma correction exponent. For CRT, $\gamma \in [1.3, 2.4]$; for other devices or if γ is unknown, search the allowed range starting from $\gamma = 1$.	[1.3, 2.4] (0, ∞)

*Description of the primary role of each heuristic parameter. For some parameters in addition to the range of values that are theoretically allowed, we report the range of suggested values that are likely to produce the best results.

direction) and φ_v (angle within the viewing plane). φ_v and θ_v are related to the 2D cylindrical coordinates ρ and of the equal area color circle as $\rho = 2\sin(\theta_v/2)$ and $\phi = \varphi_v$. Alternatively, color circles in which $\rho = \sin(\theta_v)$, or $\rho = \theta_v$, can also be constructed and are useful for an easier reading of θ_v. However, the equal area color circles provide the means to better judge the uniformity of a given color representation, and therefore we used them to calibrate the heuristic parameters.

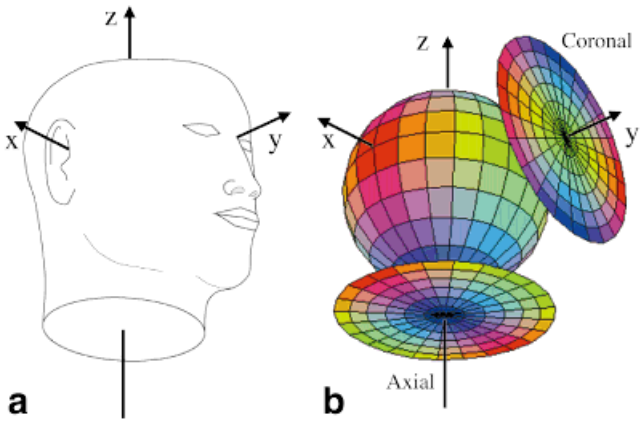

FIG. 2. **a:** Anatomic reference frame. **b:** Color representation sphere for the *absolute value* scheme. In (**b**) we show the projection of the color representation sphere onto a color circle for axial and coronal views, assuming that axial and coronal slices are exactly perpendicular to the z and y axes of the anatomical reference frame, respectively. Note that the grid for coronal view is not the projection of the constant θ and φ lines but rather the grid of constant θ_v and φ_v as defined in the text. The orientation of a structure represented with a given color, can be approximately obtained from the color circle by placing one end of a "pencil," whose length is approximately equal to the radius of the circle, at the center of the circle and the other end right above the corresponding color.

The anatomic coordinate system and the reference system for image display do not necessarily coincide, i.e., axial, coronal, and sagittal images are not lying in the xy, xz, and yz planes of the anatomical coordinate system, respectively. In such case, the color coordinate system appears shifted relative to the color circle grid (e.g., the white point in the circles in Fig. 5c, d, and e, would not be exactly in the center of the circle) and the above proposed symmetries in color representation would not be easily seen on the color circle. If the misalignment between the anatomical coordinate system and the reference system for image display is severe, images should be interpolated and redisplayed after proper rotation. However, if the misalignment is small (<10°), as in our case, errors introduced by displaying images in their original form and color circles in the anatomical reference frame are negligible.

MRI

The DEC maps presented in the figures were produced from diffusion data obtained from two 30-year-old female normal volunteers. We used a 1.5-T GE Signa Horizon EchoSpeed spectrometer (GE Medical Systems, Milwaukee, WI), equipped with a whole-body gradient coil capable of producing gradient pulses up to 22 mT/m with a slew rate of 120 T/m/s. Diffusion images were acquired with an interleaved spin-echo echo-planar imaging sequence with a navigator echo for correction of motion artifacts. A description of the algorithms used for image reconstruction is presented elsewhere (31,32). Imaging acquisition parameters for axial sections were as follow: 32 contiguous slices, 3.5-mm slice thickness, rectangular 165 × 220-mm field of view, 96 × 128 in-plane resolution (6 interleaves, 16 echoes per interleaf), repetition time of greater than 5000 msec, echo time of 78 msec, and cardiac gating (4 acquisitions per heart beat starting with a 200 ms delay after the rise of the sphygmic wave as measured

by a peripheral pulse oxymeter). Six diffusion directions were sampled using combinations of the x, y, and z physical gradients as previously described (6). Each physical gradient had a strength of 21 mT/m, yielding an effective strength of 29.7 mT/m in the sampled diffusion direction. The value of the trace of the b-matrix (33), which is equal to the effective b-value in the sampled direction, was 1000 sec/mm^2. Four images with no diffusion gradients were also acquired for a total of 28 images per slice. The imaging time for the acquisition of the entire diffusion imaging data set was about 30 min. We also acquired conventional fast spin echo T_1-, T_2-, and proton density-weighted images matching the slices of the diffusion study, having however a higher in-plane resolution (192 × 256). Following image reconstruction, we computed the b-matrix numerically for each diffusion weighted image (33). We calculated $\underline{\mathbf{D}}$ in each voxel according to Basser et al. (1,2), and generated maps of the lattice anisotropy index (20).

RESULTS

Figure 3 shows an axial section of the human brain with a conventional T_2-weighted image (Fig. 3a), a map of the lattice anisotropy index (Fig. 3b), and a line field representation of $\mathbf{V}_{max}$ visualized using a scheme similar to that presented by Tang et al. (16) (Fig. 3c). With 2D projection representations, and to a lesser extent also with representations based on 3D rendering of solids, such as diffusion ellipsoids, fiber direction is faithfully represented for structures positioned within the plane of the image, such as the corpus callosum. However, structures having a strong directional component along the viewing axis, such as the posterior limb of the internal capsule and the cingulum (arrows), are poorly represented.

Figure 4 shows the same axial section of normal human brain as in Fig. 3 using the previously proposed color representation schemes. Figure 5 shows implementation of the *absolute value* case in uniform color spaces (Fig. 5a) and several heuristic mapping schemes: *absolute value* (Fig. 5b), *rotational symmetry* (Fig. 5c), *mirror symmetry* (Fig. 5d), *no symmetry* (Fig. 5e), and the *preferred direction* (Fig. 5f) cases. The full effect of the heuristic approach, however, cannot be appreciated, since the heuristic parameter p_C was set to 0.5 (see Table 2) to yield a larger range of colors and to achieve a better match between the printed and the displayed image.

A comparison between the DEC map suggested by Pierpaoli (25), displayed with no gamma correction (Fig. 4a) and with proper gamma correction (Fig. 4b), demonstrates the importance of properly handling this parameter. The color circle of Fig. 4a has large regions predominantly colored in red, green, and blue, that are separated by narrow boundaries between them. Consequently, fiber directions in the brain image appear artifactually segmented. For example, sharp color transitions are present between the blue and green regions in the posterior limb of the internal capsule (*arrows*) as well as between the red and green regions in the genu of the corpus callosum (*arrows*), suggesting abrupt variations in fiber direction. This indeed is an artifact of the color representation because the orientation of these structures varies smoothly, as confirmed by a histogram analysis of the same data, and as can be seen by the smoother transition in Fig. 4b, where gamma correction has been properly implemented. However, the image of Fig. 4b fails to provide an accurate representation of diffusion anisotropy. By comparing Fig. 4b to Fig. 3b, which displays a gray scale map of the lattice anisotropy index for the same section, structures represented in green appear to have a higher anisotropy than they really have, whereas structures represented in blue have a lower apparent anisotropy. This problem is partially corrected in Fig. 5b using the heuristic approach. Figure 4c shows the appearance of the DEC map suggested by Jones et al. (26). In Jones' approach, voxels having a degree of anisotropy below a certain threshold (here $\Lambda_{min} = 0.15$) are not considered and are represented in black. This creates ambiguity because anisotropic structures running approximately perpendicular to the plane of the image (such as the internal capsule) are also represented in black. However, the main problem with this approach is that discontinuity artifacts are present. They consist of sharp artifactual boundaries between complementary colors occurring in structures that are approximately oriented within the plane of the image, such as the corpus callosum (*arrows* in Fig. 4c). Without prior knowledge of brain anatomy, it would be

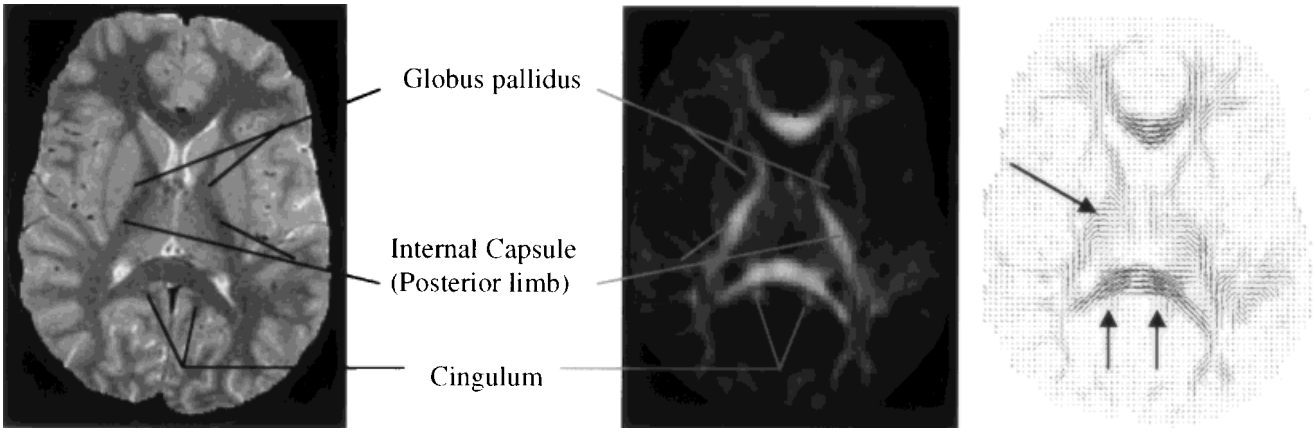

FIG. 3. (**a**) T_2-weighted image of an axial section of the human brain; (**b**) image of the lattice anisotropy index; and (**c**) in-plane projection of $\mathbf{V}_{max}$ using line fields. The length of the line segment in each voxel is linearly proportional to the lattice index.

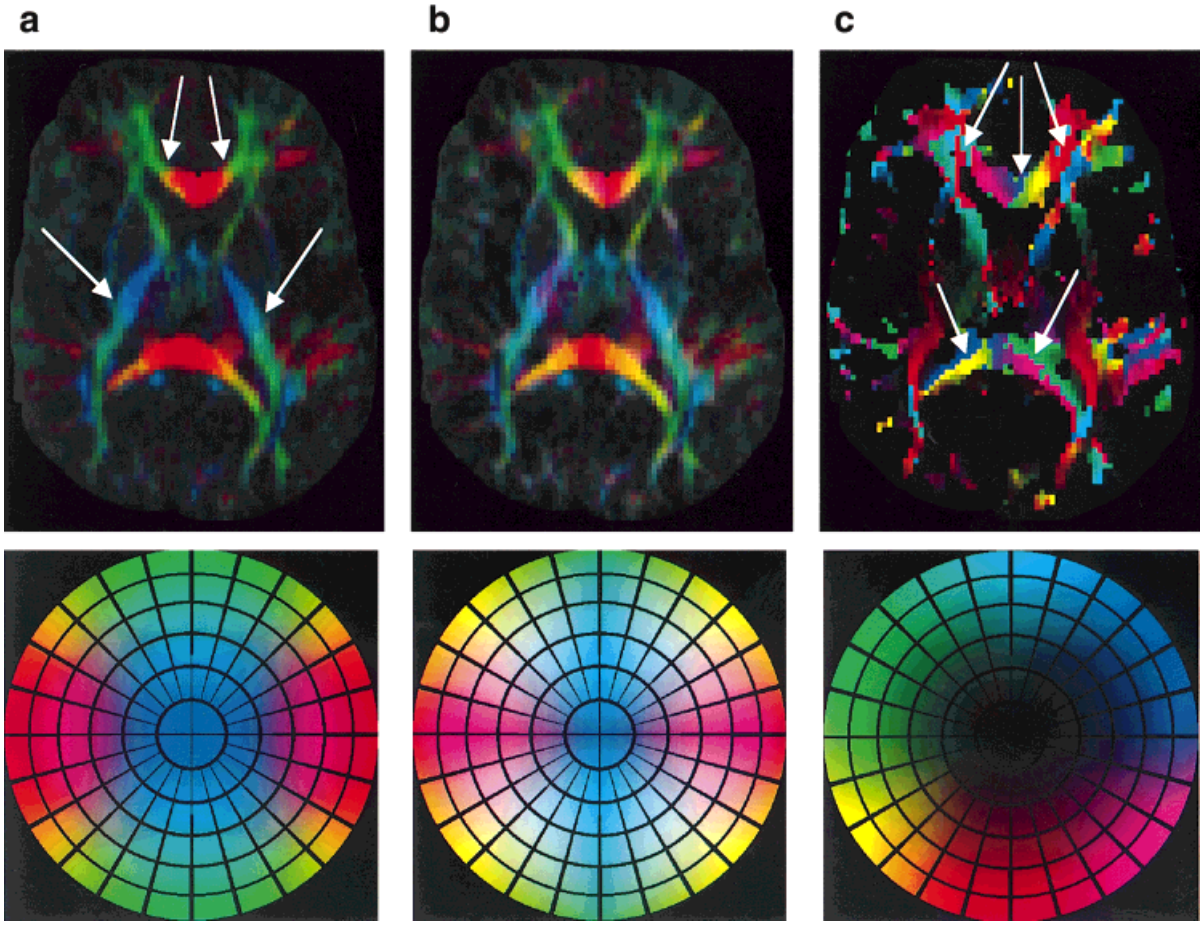

FIG. 4. Previously proposed color schemes for fiber direction mapping from diffusion tensor imaging data. The same axial section of the human brain shown in Fig. 3 is displayed using the DEC mapping scheme proposed in Ref. 25, implemented both with no gamma correction (**a**), and with the proper gamma correction (**b**). The DEC mapping scheme proposed in Ref. 26 is also shown (**c**).

impossible to discern whether these sharp color transitions are true boundaries between differently oriented structures or just artifacts of the color scheme.

Discontinuity artifacts were also present in the *mirror symmetry* (Fig. 5d) and *no symmetry* cases (Fig. 5e). Only the *rotational symmetry* (Fig. 5d) and *absolute value* (Fig. 5b) schemes were free of discontinuity artifacts. However, they do not provide a unique representation of directions; additionally, the *rotational symmetry* scheme produces a perceptually nonuniform representation (sensitivity along φ is much greater than along θ). Figure 5f shows that the *preferred direction* representation can be used to shift the discontinuity artifacts away from the structures of interest. The preferred direction that was used coincided with the average orientation of the fibers contained in the region of the corpus callosum indicated by the *arrowhead*. The black band in the color circle encompassed directions that were very close to the plane perpendicular to the preferred direction whose representations were eliminated by using the critical angle $\theta_C = 80°$ (see Appendix B). In this way any color transitions, except those between black and saturated hues, reflect true anatomical features and do not originate from discontinuity artifacts. A summary of the three important properties of the color representation: presence of discontinuity artifacts, perceptual uniformity, and presence of orientational ambiguity, is presented in Table 1 for five different representations.

Figure 6a shows a T_2-weighted image of an axial section of the pons. Figure 6b and c, show DEC maps of the same section using the *absolute value* and *no symmetry* heuristic equations, which are the least unique mapping scheme and the scheme with the worst discontinuity artifacts, respectively (see Table 1). Despite having an in-plane resolution that is higher than that of the DEC maps, the T_2-weighted image did not identify any of the white matter pathways running in the pons at this level. On the contrary, the DEC map of Fig. 6b identified the descending motor pathways, ascending sensory pathways, and transverse pontine fibers. The cerebellar peduncles (superior, middle, and inferior) can also be easily recognized in Fig. 6b. In this figure, however, the nonuniqueness of fiber direction as a result of taking the absolute value of each component of $\mathbf{V}_{\mathbf{max}}$, can be observed in some regions. For example, it can be seen that the inferior cerebellar peduncle (ICP) and superior cerebellar peduncle (SCP), which have very different orientations, appeared with similar colors. The true orientations of ICP and SCP are indicated on the corresponding color circles. These ambiguities were eliminated using the *no symmetry* approach (Fig. 6c); however, discontinuity arose at the boundary between the left ICP and adjacent

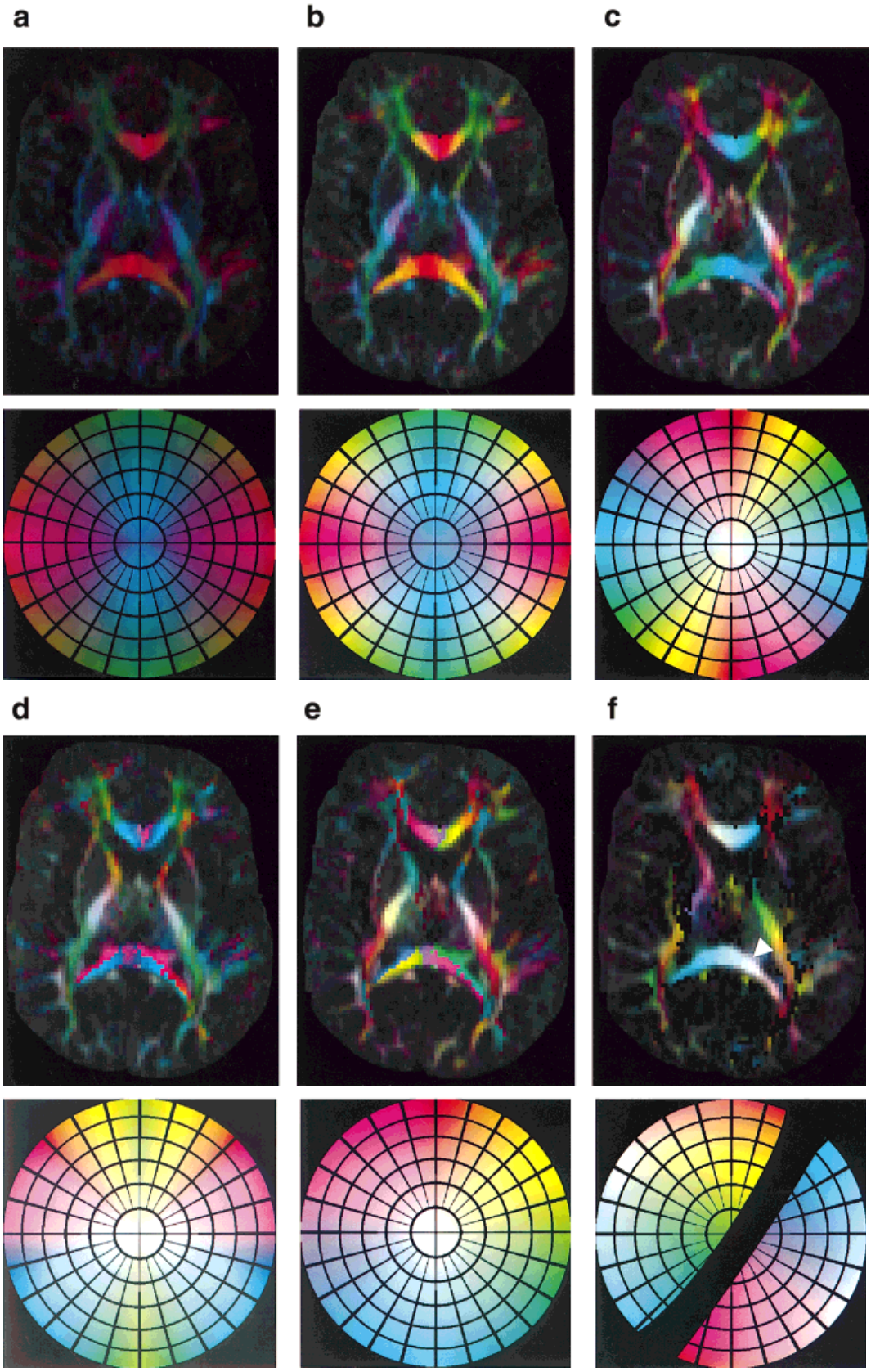

FIG. 5. Different heuristic color schemes for fiber direction mapping. Maps of the same axial section of the human brain seen in Fig. 3 are shown using the formulas for (**b**) *absolute value,* (**c**) *rotational symmetry,*(**d**) *mirror symmetry,* (**e**) *no symmetry,* and (**f**) *preferred direction.* The arrowhead in (**f**) points to the region in the splenium of the corpus callosum that defines the preferred direction used in this case. The *absolute value* case implemented in CIEL*u*v* uniform color space is also presented (**a**).

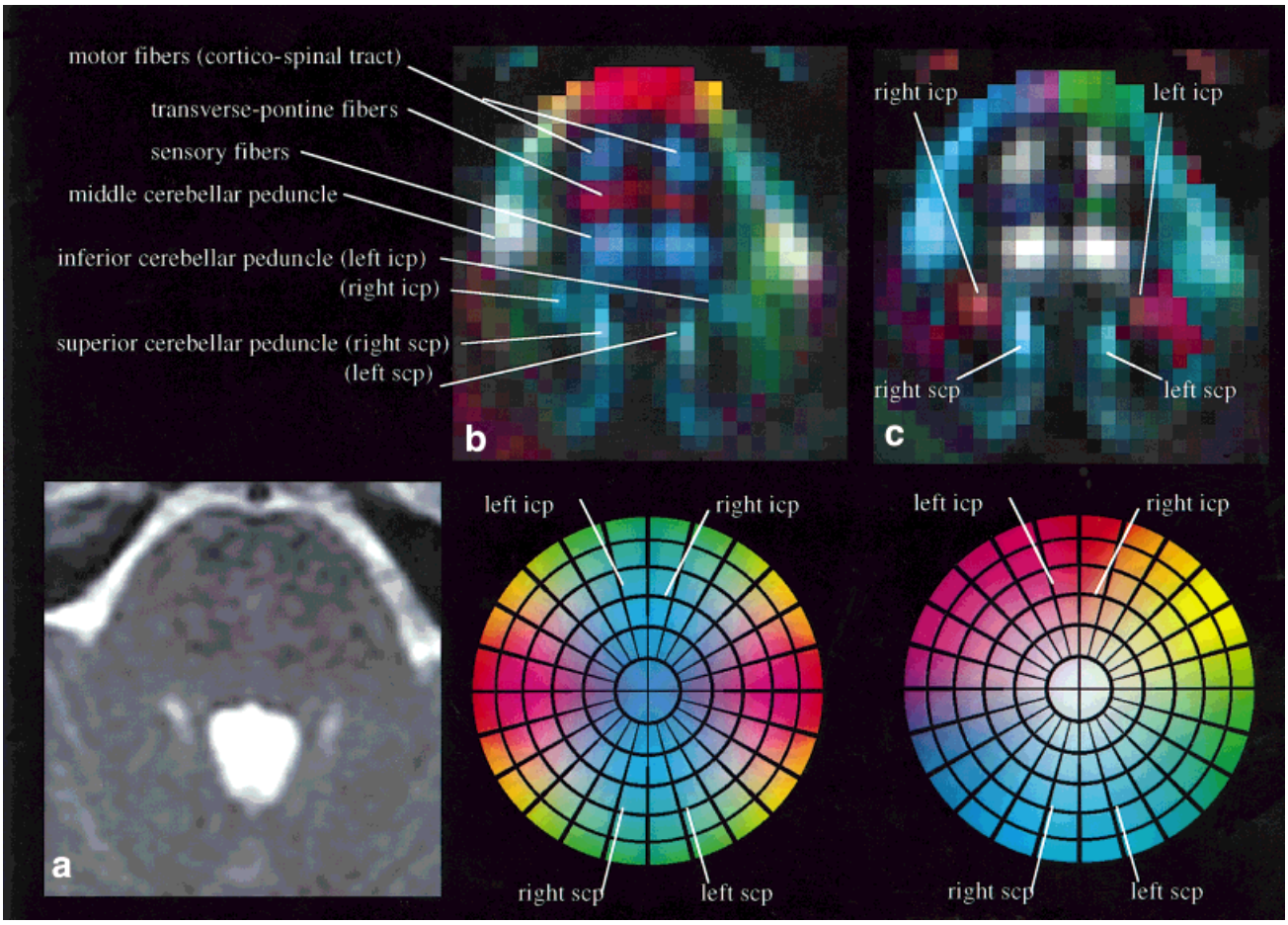

FIG. 6. Axial section of the pons as depicted by (**a**) T_2-weighted imaging, and DEC mapping using the (**b**) *absolute value* and (**c**) *no symmetry* heuristic equations.

fibers. This ambiguity can be resolved by using the *preferred direction* representation with an ROI positioned on the left ICP (not shown).

Figure 7 shows DEC maps obtained with the *absolute value* heuristic equation in five coronal sections of normal human brain. This is the DEC scheme we favored for initial viewing of fiber direction in brain imaging. Most of the main association, projection, and commissural pathways can be clearly identified in these images. It is interesting that neighboring white matter pathways having similar anisotropy (as well as similar signal intensity in conventional MRI) can be discriminated on the basis of their different directions. One interesting example is in the most posterior section (left bottom of the figure) where the optic radiation, running predominantly in an anterior-posterior direction, can be differentiated from the neighboring vertical occipital fibers oriented in a superior-inferior direction.

DISCUSSION

We have addressed the issue of representing fiber direction from diffusion tensor imaging data using colors. Compared to graphic schemes (vector fields, diffusion ellipses, octahedra, ellipsoids, etc.), color representation schemes potentially better represent fibers oriented at an angle with the plane of the image. Nevertheless, one important issue in color representation is to preserve the quantitative nature of the directional information contained in the diffusion tensor. In this paper, we identified and described three main sources of artifacts in previously proposed DEC schemes: (i) nonlinear effects of the display device; (ii) properties of human color perception; and (iii) antipodal symmetry of the eigenvectors of $\mathbf{D}$

(see the Background section). While (i) can be corrected, (ii) and (iii) pose fundamental limitations to achieving the ideal case of having perceived color differences proportional to the actual differences in direction.

It is a natural tendency of the human visual system to interpret separate regions with similar colors as belonging to the same object or structure. Thus, it is insufficient just to assign different colors to different directions and the perceived differences between the colors must also be taken into account. Although perceptually uniform color spaces can be constructed, their validity is limited when applied to complex color images. Additionally, the constraint of uniformity requires omitting a significant range of colors (see Appendix C and Fig. 5a), thus producing an unsatisfactory representation. Therefore, we favor an empirical or heuristic approach to the issues of color perception. For a given display device, we found that a perceptu-

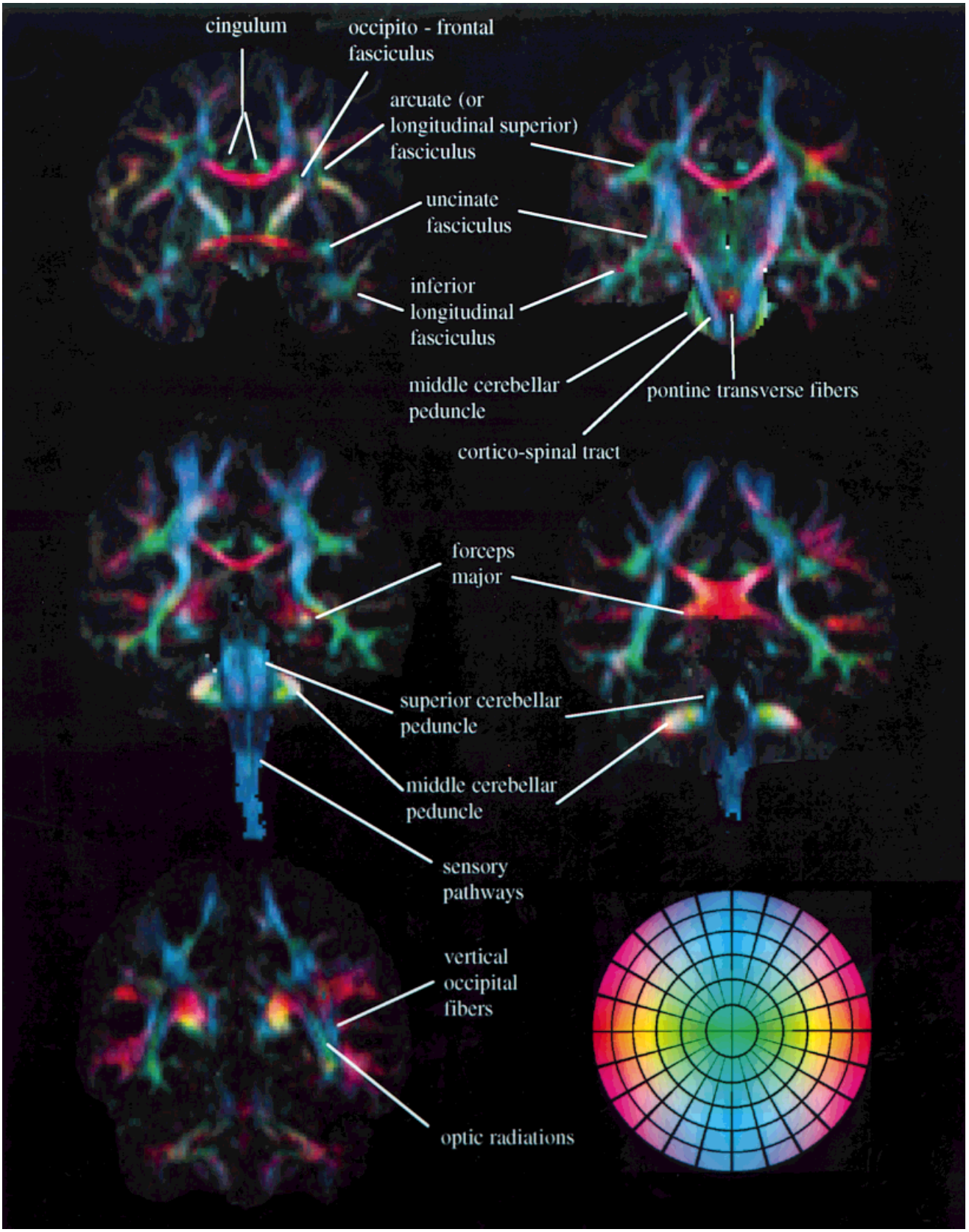

FIG. 7. Set of coronal DEC maps constructed using the *absolute value* heuristic equation. All the main association, projection, and commissural pathways can be easily identified in these images. The color circle for coronal images has a different appearance from that used for axial images. This is because the DEC mapping scheme is defined in an anatomic coordinate reference system so that each structure maintains its color independently from the viewing angle, while the color circle is constructed to allow identification of directions in the reference frame of the plane in which the image is displayed, as described in Materials and Methods and in Fig. 2.

ally satisfactory representation could be obtained by adjusting the heuristic parameters and judging interactively the effects on the color circle which maps all possible directions. This approach is described in detail in Appendix A and Table 2. Improvements over previously proposed schemes are shown in the Results section. By expressing the colors obtained in a heuristic representation with L*u*v* components of CIEL*u*v* space, the improvements over previously used schemes can be assessed quantitatively. For example, in trying to achieve the goal that perceived brightness indicates the degree of anisotropy, we want regions of constant anisotropy to correspond to regions of constant perceived brightness. When the anisotropy weighting factor Λ_w is set to 1, for example, each color is set to its maximal brightness, the range of perceived brightness for different directions/colors is very large when no heuristic corrections are performed. In this case the perceived brightness ranged from $L^* = 0.4$ for the blue to $L^* = 1$ for white ($L^* = 0$ is black). When heuristic corrections were used ($p_C = 1$, $p_B = 0.2$, $p_E = 1$, $L_E = 0.6$), this range was much narrower ($L^* \in [0.59,0.63]$) indicating much better uniformity in the perceived brightness for the constant anisotropy index. Another significant limitation in achieving a quantitative color representation is related to the antipodal symmetry of the eigenvectors of $\underline{\mathbf{D}}$. The problem stems from the fact that the antipodally symmetric directional data (axial data) cannot be mapped into a continuous metric space. If one tries to construct a representation in which a given color uniquely corresponds to a given direction, a discontinuity in the representation occurs resulting in artificial boundaries or undesirable speckled patterns (Figs. 4c and 5d and e). Schemes that assume rotational symmetry can alleviate this problem but they do not offer a unique color representation of directions (see Table 1). Another approach is to selectively represent structures by using the *preferred direction* scheme. When using the *preferred direction* scheme, one can be confident that boundaries between colored (nonblack) regions indicate true differences in direction, provided that θ_C is set sufficiently smaller than 90°. Only the boundaries between the black and saturated hues may be artifacts because black regions may represent either anisotropic structures lying close to the plane of discontinuity or isotropic tissue. This approach is best used for selective viewing within an ROI to visualize the orientation of a particular structure without ambiguity or artifacts.

THE DEC MAPS PROTOCOL

From the above, it is evident that using only a single DEC map leads to ambiguities and misrepresentation. We propose using different representation schemes to address each of the problems separately. The protocol that we implemented in our Institution enables one to use any of the mentioned coloring schemes and to choose between truncation or weighting with a rotationally invariant anisotropy index, such as the lattice index. We used the heuristic *absolute value* (Fig. 5b) and *rotational symmetry* (Fig. 5b) schemes to view initially brain images. Although these schemes do not provide a unique representation of fiber direction, they are void of discontinuity artifacts. The *rotational symmetry* cheme has a less ambiguous (more unique) representation of directions than the *absolute value* scheme because one color represents two directions instead of four. However, its discriminative power for angles in the polar (θ) direction is poorer than in the azimuthal (φ direction, a disadvantage not present in the *absolute value* scheme. For a more detailed representation of fiber direction, images were also viewed with the heuristic *no symmetry* (Fig. 4c) scheme. Once a particular fiber tract is to be analyzed, we determined its average direction in a small ROI and used the *preferred direction* (Fig. 4d) scheme to further improve visualization of both the tract and similarly oriented neighboring structures.

Although we chose this protocol to work with brain images, alternative approaches may be more appropriate for other tissues and organs. For example, for images of the heart on sections perpendicular to the long axis, the *rotational symmetry* scheme may be optimal because of the directional arrangement of cardiac fibers.

OTHER ISSUES

In regions where the diffusion ellipsoids are prolate (cigar shaped), it is reasonable to assume that the fiber orientation is determined by the eigenvector associated with the largest eigenvalue, $\mathbf{V}_{max}$. However, in regions where diffusion ellipsoids are oblate and axisymmetric (pancake shaped), using $\mathbf{V}_{max}$ to indicate fiber direction is meaningless because $\mathbf{V}_{max}$ is randomly oriented within the plane perpendicular to the direction of the smallest diffusivity. Some regions of the brain indeed have an architectural arrangement of fibers resulting in a diffusion displacement profile described approximately by oblate ellipsoids (6). Because these regions correspond to highly negative values of the skewness of the eigenvalues (15,34), filtering by the skewness of the eigenvalues could be implemented, just as we used an index of diffusion anisotropy to mask voxels where diffusion is isotropic.

Implementation of our formulas is mainly intended for the 24-bit color graphics CRT devices, which we used in this work. If an 8-bit color display with a maximum of 256 colors has to be used, one needs to resort to sophisticated dithering schemes to achieve satisfactory results. If this is unavailable through display software, we suggest implementing a less accurate scheme that is a simple discretization of the above- mentioned representations. In it, the number of the discrete cells for vector representation has to be equal or smaller than the number of available colors, otherwise, colors will be approximated with the closest available ones and this often produces significant distortion. We viewed images only with 24-bit graphics cards. When printing images, we used the printer driver to perform device-independent color correction, including correction for the difference between the gamma exponents. Even high-quality color printers, however, cannot produce printouts of images that faithfully reproduce what one sees on the computer screen. It should be considered that our description of the figures is based on their appearance on the screen and their reproduction in the final print may not be accurate.

CONCLUSIONS

DEC maps can be used to represent the orientational information contained in the diffusion tensor. We identi-

fied several desirable properties that DEC mapping schemes should possess in order to provide a satisfactory representation of fiber direction. We also identified sources of errors that arose in representing this information using color. These are related to the discontinuity artifacts resulting from the antipodal symmetry of eigenvector data as well as to the display and perception of colors. The goal of having a representation in which perceived color distances are proportional to the actual differences in orientation is, generally, not achievable. Based on our investigation and experience in working with DEC maps, we recommend that perceptual properties of human vision and the nonlinear properties of the display devices be handled through an heuristic approach. A set of heuristic parameters is calibrated (tuned) by using color circles that are equal area projections of the color representation sphere, and by searching for a perceptually satisfactory representation on a given device. Discontinuity artifacts can be mitigated by taking advantage of symmetries encountered in the tissue, or by selecting a preferred direction so that the structure of interest is oriented perpendicular to the plane of discontinuity. The main goal of this work was not to suggest a particular implementation, but rather to address general issues involved in color representation of fiber direction that are relevant when constructing the appropriate DEC protocol for a particular imaging situation. Finally, by using our color approach to map white matter fiber tracts in the human brain, we have clearly identified the location and orientation of several white matter pathways which were not previously mapped in vivo using a noninvasive technique.

APPENDIX A: IMPLEMENTATION OF THE HEURISTIC APPROACHES

Color Maps of $\mathbf{V}_{max}$

Here, we map the vector $\mathbf{V}_{max}(v_x, v_y, v_z)$, or $\mathbf{V}_{max}(\theta,\varphi)$, into a RGB color space. Let R_I, G_I, and B_I be the RGB components of the color representation of $\mathbf{V}_{max}$, which are defined in the interval [0, 1]. In most schemes, R_I, G_I, and B_I are obtained from HSV (Hue, Saturation, Value) components using the standard HSV to RGB conversion (28). The implementation of the color maps based on the four symmetries described in Materials and Methods are as follows:

No Symmetry

$$H = (\varphi - \varphi_R + 2\pi) \bmod 2\pi$$

$$S = \frac{\sin(p_s\theta)}{\sin(p_s\pi/2)}$$

$$V = 1 \qquad [A1]$$

in which φ_R is the φ angle of the vector lying in the xy plane that will be represented in a pure red color, and $p_S \in [0,1]$ is an heuristic parameter (e.g., $p_S = 0.5$ in Fig. 5.c) . When $p_S \approx 0$, S is approximately a linear function of θ. For the next two representations the S and V are the same as in [A1] and H is as follows:

Rotational Symmetry

$$H = 2(\varphi - \varphi_R + 2\pi) \bmod 2\pi \qquad [A2]$$

Mirror Symmetry
φ is azimuthal angle of $\mathbf{V}_{max}(|v_x|, v_y, v_z)$

$$H = 2((\varphi - \varphi_R + \pi) \bmod \pi) \qquad [A3]$$

The formulas for the H, S, and V components in the *preferred direction* approach are described separately in Appendix B. In the *absolute value* approach R_I, G_I, and B_I are obtained directly as:

Absolute value

$$R_I = |v_x|$$

$$G_I = |v_y|$$

$$B_I = |v_z| \qquad [A4]$$

Anisotropy Filter

We allowed the brightness of a given color to be modulated by the degree of anisotropy. We implemented two types of anisotropy filters in our color representations. In the first one, each of the color components contains a weighting factor Λ_w of the form $\Lambda_w = \max[0, \min(1, \Lambda - \Lambda_{min})/(\Lambda_{max} - \Lambda_{min})]$, where Λ_{min} and Λ_{max} delimit the range of values of the lattice index within which the weighting factor linearly increases from 0 to 1. In the second, only structures where the lattice index was larger than Λ_{min} are represented, the others are truncated and set to black. In schemes based on perceptually uniform color spaces, the weighting by lattice index is included within the representation model, e.g., luminosity $L^* \sim \Lambda_w$. This is the only correct way to preserve the perceptual uniformity after the filtering by Λ_w. In the heuristic schemes, we added an heuristic correction to the simple multiplication by Λ_w, which yielded acceptable results (see the following subsection).

Heuristic Corrections

In this section, the R_I, G_I, and B_I are further processed to produce a representation in which heuristic parameters p_B, p_E, L_E, p_β, p_S, and p_C are applied to improve the color representation. We also treated the gamma correction exponent ($\gamma \cong 2.2$) and the Steven's law exponent ($\beta \cong 0.4$) as heuristic parameters, i.e., we allowed them to be empirically adjusted. In our approach we tried to preserve the intuitive character of color representation and to remove some artifacts in a simple way using only a few free parameters. Regarding the nonuniformity in perceived distances, the most significant factor was improper implementation of the gamma correction. Parameters γ and p_S were specifically used for modification of color uniformity, and together with other heuristic parameters, produced a satisfactory level of uniformity. Any more elaborate scheme would require abandoning the goal of obtaining an intuitive association between typical color groups and directions [see (d) in Background]. This goal, for example, is not

achieved with schemes based on uniform color spaces. Also significant is the difference in perceived brightness between different hues. Perceived brightness for maximum value of pure red, green, and blue components, according to CIEL*u*v* color space for our computer monitor, are approximately 0.4, 0.6, and 0.8, respectively; and for yellow, cyan, and magenta, $L^* \cong 0.95$, 0.87, and 0.7 ($L^* = 0$ is black, $L^* = 1$ is white). We found that the perceived brightness can be approximated according to $L^* = (0.3R + 0.59G + 0.11B)^{0.4}$, where L*, R, G, and B are all mapped into the interval [0,1]. This approximation is valid for a wide range of colors for which $L^* > 0.1$ and is derived from the CIE specifications for our computer screen. Knowing this, we derived a scaling factor F_L which, when applied to RGB components, brought all color compositions to the same brightness L_E. The choice of L_E had to be high enough to produce an image with sufficient brightness, but low enough to include a wide range of colors. We chose a moderately high value for L_E in the range $L_E \in (0.6, 0.8)$. Since some color compositions cannot achieve this brightness, we shifted the blue component, and also for $L_E > 0.7$ the red component, toward the white point. The higher the value of L_E the larger the shift that was required. Uniform brightness is important when one wants to view the directional information and the degree of anisotropy simultaneously. In other situations, when the degree of anisotropy is less important one may use a larger range of colors. This is governed by the parameter p_C. In the first step of implementation we shifted ''blue'' toward the white point according to:

$$
\begin{aligned}
R_S &= C_B B_I + (1 - C_B) R_I \\
G_S &= C_B B_I + (1 - C_B) G_I \\
B_S &= B_I \\
C_B &= \max\left[\frac{3}{2}\, p_B \left(b - \frac{1}{3}\right) p_C,\, 0\right] \\
b &= \frac{B_I}{R_I + G_I + B_I}
\end{aligned}
\qquad [A5]
$$

In the same manner, we modified R_S, G_S, and B_S by shifting the red component but with a smaller shift (p_R ($p_B/4$). From the R_S, G_S, and B_S values we obtained the digital values f_r, f_g, f_b to be stored in the frame buffer of the display device according to:

$$
\begin{aligned}
f_r &= F_{max}\left(\Lambda_w^{p_\beta} \frac{R_S}{L_F}\right)^{1/\gamma} \\
f_g &= F_{max}\left(\Lambda_w^{p_\beta} \frac{G_S}{L_F}\right)^{1/\gamma} \\
f_b &= F_{max}\left(\Lambda_w^{p_\beta} \frac{B_S}{L_F}\right)^{1/\gamma}
\end{aligned}
\qquad [A6]
$$

where F_{max} is the largest integer that can be stored in each of the color channels (for 24-bit display, the channels have 8-bit registers and thus $F_{max} = 255$); Λ_w is the weighting factor based on the lattice index; and L_F is the scaling factor obtained by using the heuristic parameters L_E, p_C and p_E as follows:

$$
\begin{aligned}
L_F &= p_C F_L + (1 - p_C) L_M \\
F_L &= \min\left[\frac{c_1 R_S + c_2 G_S + c_3 B_S}{L_E^{1/\beta}},\, 1\right] \\
L_M &= \max\left[R_B, G_B, B_B\right] \\
c_1 &= \frac{1}{3} - \frac{p_E}{25} \\
c_2 &= \frac{1}{3} + \frac{p_E}{4} \\
c_3 &= 1 - c_1 - c_2
\end{aligned}
\qquad [A7]
$$

where $\beta \cong 0.4$ can be treated as an heuristic parameter. In addition, equations for constants c_1, c_2, and c_3 can be varied if a non-CRT based display device is used. The form of Eq. [A6] is based on gamma correction and also includes the anisotropy filtering by Λ_w. If truncation is preferred instead, complete exclusion of voxels having anisotropy below a certain threshold Λ_{min} with no weighting for the remaining voxels is obtained by setting the factor $\Lambda_w^{P_\beta} = 1$ if $\Lambda > \Lambda_{min}$, otherwise $\Lambda_w^{P_\beta} = 0$.

APPENDIX B: IMPLEMENTATION OF THE PREFERRED DIRECTION SCHEME

Let us assume that the preferred direction is described by a vector $\mathbf{v}_p \equiv \{x_p, y_p, z_p\}$. We want to express the original polar and azimuthal angles θ and φ as angles θ_p and φ_p, which are corresponding angles in the new coordinate system in which the z axis coincides with $\mathbf{v}_p$. For an arbitrary vector $\mathbf{v}$ we derive θ_p and φ_p according to

$$
\theta_p = \mathrm{ArcCos}\,|\mathbf{v} \cdot \mathbf{v}_p|
$$

$$
\varphi_p = \begin{cases}
\mathrm{ArcCos}\,\dfrac{(\mathbf{v}_p \times \mathbf{v}) \cdot \hat{\mathbf{n}}_\varphi}{|\mathbf{v}_p \times \mathbf{v}|}, & \mathbf{v} \cdot \hat{\mathbf{n}}_\varphi > 0,\ \mathbf{v}_p \neq \mathbf{v} \\
2\pi - \mathrm{ArcCos}\,\dfrac{(\mathbf{v}_p \times \mathbf{v}) \cdot \hat{\mathbf{n}}_\varphi}{|\mathbf{v}_p \times \mathbf{v}|}, & \mathbf{v} \cdot \hat{\mathbf{n}}_\varphi < 0,\ \mathbf{v}_p \neq \mathbf{v} \\
0 & \mathbf{v}_p = \mathbf{v}
\end{cases}
\qquad [A8]
$$

where $\hat{\mathbf{n}}_\varphi$ is the unit vector defining a normal to the plane which contains vector $\mathbf{v}_p$ and defines a plane of vectors for which $\varphi_p = 0$, or $\varphi_p = \pi$. We choose such a plane to be

defined by $\mathbf{v}_p$ and the y axis, i.e.:

$$\hat{\mathbf{n}}_\varphi = \begin{cases} \dfrac{\mathbf{v}_p \times \hat{\mathbf{y}}}{|\mathbf{v}_p \times \hat{\mathbf{y}}|} & \mathbf{v}_p \neq \hat{\mathbf{y}} \\ \hat{\mathbf{x}} & \mathbf{v}_p = \hat{\mathbf{y}} \end{cases}$$

where $\hat{\mathbf{x}}$ and $\hat{\mathbf{y}}$ are the unit vectors defining the x and y axes. The polar and azimuthal angles in the rotated coordinate system, θ_p and φ_p, are then used with HSV-based color as an heuristic approach with no symmetry, with the additional parameter θ_C used to mask the discontinuity artifacts present in the image. For $\theta_p \leq \theta_C$:

$$H = (\varphi_p - \varphi_R + 2\pi) \bmod 2\pi$$

$$S = \frac{\sin(p_S s_N \theta_p)}{\sin(p_S \pi/2)}$$

$$V = 1$$

$$s_N = \frac{\pi}{2\theta_C} \qquad [A9]$$

and for $\theta_p > \theta_C$ we set $V = 0$. For $\theta_p > \theta_C$ we also allow that both V and S are smoothly decreased according to $S,V = [1-(\theta_p - \theta_C)/(\pi/2 - \theta_C)]^D$, $D > 2$ controls the smoothness of transition. The latter case offers a visually more pleasing representation; however, if multiplicative scaling with a lattice index is used there is ambiguity between the structures with low anisotropy and those outside the cone defined by θ_C.

APPENDIX C: IMPLEMENTATION OF THE UNIFORM COLOR SPACE APPROACH

We omitted the many details of our implementations because of the space that it would require, and because of the unsatisfactory results that this approach produces. In addition, we did not describe the transformations that map between RGB space of a given display device and CIEL*u*v* uniform color space (27). These require precise CIE specifications for a given display device to be known which can sometimes be obtained only by direct calibration. Once the mapping between the RGB and CIEL*u*v* spaces was obtained, we could express $\mathbf{V}_{max}$ in terms of L*, u*, and v* (approximately Euclidean coordinates). The task, however, is not straightforward, since embedding a regular coordinate system, in which $\mathbf{V}_{max}$ is represented, within the irregular boundaries of the displayable colors (color gamuts) in the uniform color space requires omission of a significant range of colors. Only the *no symmetry* case can be implemented in a relatively straightforward way by using perceptual correlates of hue, saturation, and brightness (27), but still sacrificing a significant range of colors. The *absolute value* scheme was implemented by choosing a plane of constant perceived brightness $L^* = L_E\Lambda_w$ in the CIEL*u*v* space. This plane was then projected onto an octant of a sphere using the azimuthal equidistant projection (distortion due to such projection in this case is relatively small). Here, too, the irregular boundaries of the planar color gamut within the extracted plane limited the range of colors to be used and additionally L_E had to be set sufficiently low ($L_E < 0.6$) in order to have acceptable color gamuts for all Λ_w. This is why the images obtained within this approach appear dark and not very colorful. This can be improved by abandoning the goal of relating the degree of anisotropy to the perceived brightness in which case an oblique plane extracted from the CIEL*u*v* space will be mapped on the color representation sphere. Constraints of rotational, and to a lesser degree mirror symmetry, introduce significant distortions from uniformity and thus are not practical to implement using the uniform color spaces. Thus, this approach suffers from the difficulties of having to implement a device-independent color representation properly, and to embed a regular coordinate systems into the irregular boundaries of color gamuts of the uniform color spaces without significantly reducing the range of colors used. We have omitted the many details of our implementations because of the space that it would require, and because of the unsatisfactory results that this approach produces. The results for this approach require that all color parameters of the final printing device be known. Since these were unavailable, Fig. 5a is not truly a uniform color space implementation. Images presented in this paper can be found at http://mscl.cit.nih.gov/spaj/dti for viewing on a CRT device.

REFERENCES

1. Basser PJ, Mattiello J, LeBihan D. Estimation of the effective self-diffusion tensor from the NMR spin echo. J Magn Reson B 1994;103:247–254.
2. Basser PJ, Mattiello J, LeBihan D. MR diffusion tensor spectroscopy and imaging. Biophys J 1994;66:259–267.
3. Basser PJ. Inferring microstructural features and the physiological state of tissues from diffusion-weighted images. NMR Biomed 1995;8:333–344.
4. van Gelderen P, de Vleeschouwer MH, DesPres D, Pekar J, van Zijl PC, Moonen CT. Water diffusion and acute stroke. Magn Reson Med 1994;31:154–163.
5. Ulug AM, Beauchamp N Jr, Bryan RN, van Zijl PC. Absolute quantitation of diffusion constants in human stroke. Stroke 1997;28:483–490.
6. Pierpaoli C, Jezzard P, Basser PJ, Barnett A, Di Chiro G. Diffusion tensor MR imaging of the human brain. Radiology 1996;201:637–648.
7. Pierpaoli C, Barnett A, Virta A, Penix L, Chen R. Diffusion MRI of Wallerian degeneration. A new tool to investigate neural connectivity in vivo? In: ISMRM Proceedings, Sydney, Australia, 1998. p 1247.
8. Garrido L, Wedeen VJ, Kwong KK, Spencer UM, Kantor HL. Anisotropy of water diffusion in the myocardium of the rat. Circ Res 1994;74:789–793.
9. Reese TG, Weisskoff RM, Smith RN, Rosen BR, Dinsmore RE, Wedeen VJ. Imaging myocardial fiber architecture in vivo with magnetic resonance. Magn Reson Med 1995;34:786–791.
10. van Doorn A, Bovendeerd PH, Nicolay K, Drost MR, Janssen JD. Determination of muscle fibre orientation using Diffusion-Weighted MRI [published erratum appears in Eur J Morphol 1996;34:325]. Eur J Morphol 1996;34:5–10.
11. Hsu EW, Muzikant AI, Matulevicius SA, Penland RC, Henriquez CS. Magnetic resonance myocardial fiber-orientation mapping with direct histological correlation. Am J Physiol 1998;5:1627–1634.
12. Makris N, Worth AJ, Sorensen AG, Papadimitriou GM, Wu O, Reese TG, Wedeen VJ, Davis TL, Stakes JW, Caviness VS, Kaplan E, Rosen BR, Pandya DN, Kennedy DN. Morphometry of in vivo human white matter association pathways with diffusion-weighted magnetic resonance imaging. Ann Neurol 1997;42:951–962.
13. Peled S, Gudbjartsson H, Westin CF, Kikinis R, Jolesz FA. Magnetic resonance imaging shows orientation and asymmetry of white matter fiber tracts. Brain Res 1998;780:27–33.

14. Ulug A, Bakht O, Bryan R, van Zijl P. Mapping of human brain fibers using diffusion tensor imaging. In: ISMRM Proceedings, New York, 1996. p 1325.
15. Conturo TE, McKinstry RC, Akbudak E, Robinson BH. Encoding of anisotropic diffusion with tetrahedral gradients: a general mathematical diffusion formalism and experimental results. Magn Reson Med 1996;35:399–412.
16. Tang CY, Lu D, Wei TC, Spiegel J, Atlas S, Buchsbaum MS. Image processing techniques for the eigenvectors of the diffusion tensor. In: ISMRM Proceedings, Vancouver, Canada, 1997. p 2054.
17. Davis T, Van Wedeen J, Weisskoff R, Rosen B. White matter tract visualization by echo-planar MRI. In: SMRM Proceedings, New York, 1993. p 289.
18. Basser PJ, Mattiello J, LeBihan D. MR imaging of fiber-tract direction and diffusion in anisotropic tissues. In: Proceedings of the 12th Annual Meeting of the SMRM, New York, 1993. p 288.
19. Basser PJ, Mattiello J, LeBihan D. Anisotropic diffusion: MR diffusion tensor imaging. In: LeBihan D, ed. Diffusion and perfusion magnetic resonance imaging. Applications to functional MRI. New York: Raven Press; 1995. p 140–149.
20. Pierpaoli C, Basser PJ. Toward a quantitative assessment of diffusion anisotropy [published erratum appears in Magn Reson Med 1997;37: 972]. Magn Reson Med 1996;36:893–906.
21. Douek P, Turner R, Pekar J, Patronas N, Le Bihan D. MR color mapping of myelin fiber orientation. J Comput Assist Tomogr 1991;15:923–929.
22. Coremans J, Luypaert R, Verhelle F, Stadnik T, Osteaux M. A method for myelin fiber orientation mapping using diffusion-weighted MR images. Magn Reson Imaging 1994;12:443–454.
23. Nakada T, Matsuzawa H. Three-dimensional anisotropy contrast magnetic resonance imaging of the rat nervous system: MR axonography [published erratum appears in Neurosci Res 1995;23:229–230]. Neurosci Res 1995;22:389–398.
24. Inglis BA, Yang L, Wirth ED, Plant D, Mareci TH. Diffusion anisotropy in excised normal rat spinal cord measured by NMR microscopy. Magn Reson Imaging 1997;15:441–450.
25. Pierpaoli C. Oh no! One more method for color mapping of fiber tract direction using diffusion MR imaging data. In: ISMRM Proceedings, Vancouver, Canada, 1997. p 1741.
26. Jones D, Williams S, Horsfield M. Full representation of white-matter fibre direction on one map via diffusion tensor analysis. In: ISMRM Proceedings, Vancouver, Canada, 1997. p 1743.
27. Stiles WS, Wyszecki G. Color science: concepts and methods, quantitative data and formulae, 2nd edition. New York: John Wiley & Sons; 1982.
28. Foley JD, v. Dam A, Feiner SK, Hughes JF. Achromatic and colored light. Computer graphics: principles and practice. Reading, MA: Addison-Wesley; 1990. p 563–604.
29. Motta RS, Berns RS, Gorzynski ME. CRT colorimetry. Part I: Theory and practice. Color Res Appl 1993;18:299–314.
30. Land E. Recent advances in retinex theory. Vision Research 1986;26: 7–21.
31. Barnett A. Improved reconstruction algorithm for navigator corrected diffusion weighted interleaved echo-planar images. In: ISMRM Proceedings, Vancouver, Canada, 1997. p 1727.
32. Jezzard P, Barnett AS, Pierpaoli C. Characterization of and correction for eddy current artifacts in echo planar diffusion imaging. Magn Reson Med 1998;39:801–812.
33. Mattiello J, Basser PJ, Le Bihan D. The b matrix in diffusion tensor echo-planar imaging. Magn Reson Med 1997;37:292–300.
34. Basser PJ. New histological and physiological stains derived from diffusion-tensor MR images. Ann NY Acad Sci 1997;820:123–138.